

## APPLIED PHYSICS

## Fully rubbery integrated electronics from high effective mobility intrinsically stretchable semiconductors

Kyoseung Sim<sup>1</sup>, Zhoulyu Rao<sup>1</sup>, Hae-Jin Kim<sup>2,3</sup>, Anish Thukral<sup>2</sup>, Hyunseok Shim<sup>1</sup>, Cunjiang Yu<sup>1,2,4,5\*</sup>

An intrinsically stretchable rubbery semiconductor with high mobility is critical to the realization of high-performance stretchable electronics and integrated devices for many applications where large mechanical deformation or stretching is involved. Here, we report fully rubbery integrated electronics from a rubbery semiconductor with a high effective mobility, obtained by introducing metallic carbon nanotubes into a rubbery semiconductor composite. This enhancement in effective carrier mobility is enabled by providing fast paths and, therefore, a shortened carrier transport distance. Transistors and their arrays fully based on intrinsically stretchable electronic materials were developed, and they retained electrical performances without substantial loss when subjected to 50% stretching. Fully rubbery integrated electronics and logic gates were developed, and they also functioned reliably upon mechanical stretching. A rubbery active matrix based elastic tactile sensing skin to map physical touch was demonstrated to illustrate one of the applications.

## INTRODUCTION

Rubber-like electronics that can be reversibly stretched and relaxed are in high demand for a wide range of applications such as deployable structures, e-skins, wearables, medical patches, etc. In particular, rubber-like electronics at integrated levels such as active matrix electronics and interfacing and processing circuits are key components in enabling these applications to achieve their functions. While rubber-like electronic materials including conductors and semiconductors are generally needed, stretchable semiconductors with high carrier mobility are particularly crucial to realize rubber-like integrated electronics. Although there have been extensive reports on stretchable conductors (1–3), achieving a stretchable semiconductor with high carrier mobility has been a long-standing hurdle. Conventional and emerging semiconductors ranging from single-crystal inorganics to organics and to amorphous ceramics [e.g., Si, poly(3-hexylthiophene-2,5-diyl) (P3HT), rubrene, and indium gallium zinc oxide] are not mechanically stretchable (4–7). Existing strategies to make intrinsically nonstretchable semiconductors stretchable mainly involve circumventing the intrinsic material property limitations by creating mechanical structures or architectures in these materials, such as out-of-plane wrinkles (8–10), in-plane serpentine (11, 12), rigid islands with deformable interconnects (13–15), and kirigami architectures (16–18), to eliminate mechanical strain while they are stretched. While they have been successfully implemented for many applications (11, 12, 15, 18), these structured semiconductors usually involve complex fabrication, challenging packaging, and high cost. Recently developed intrinsically stretchable polymer semiconductors (19–23) suggest a suitable option for stretchable electronics. However, the development of these materials and integrated devices is still nascent:

These materials have relatively low carrier mobility [e.g., field effect mobility ( $\mu_{FE}$ ) of  $\sim 1 \text{ cm}^2/\text{V}\cdot\text{s}$ ], and integrated electronics have not been realized. To make integrated electronics in rubber format a truly viable technology it is necessary to have an intrinsically stretchable semiconductor that offers high carrier mobility, potential for scalable manufacturing, and uniformity in device performance.

Here, we introduce a stretchable rubbery semiconductor with a high effective mobility and report on fully rubbery transistors and integrated electronics and circuits. The stretchable rubbery semiconductor exploits  $\pi$ - $\pi$  stacking P3HT–nanofibrils (NFs) percolated in a silicone matrix (20). We use metallic carbon nanotubes (m-CNTs) as surface dopants, which substantially enhance the effective carrier mobility by offering superior carrier transportation paths to shorten the transport distance within the channel. This similar effective mobility enhancement has been realized in other rigid semiconductors (24, 25). The m-CNT doping was realized by dry transfer, which preserves the crystallinity of the P3HTs–NFs. The clear merits of such a high mobility intrinsically stretchable semiconductor include the following: (i) a much higher effective mobility ( $\mu_{FE}$  of  $\sim 9.76 \text{ cm}^2/\text{V}\cdot\text{s}$ ); (ii) fabrication based on commercially available precursors without further synthesizing steps; (iii) simple, repeatable, and scalable processes; and (iv) low cost. Transistors and their arrays are all made from rubber-like materials, including the m-CNT–doped P3HT–NFs/PDMS (polydimethylsiloxane) composite as a semiconductor and Au nanoparticles with conformally coated silver nanowires (AuNPs–AgNWs) embedded in the elastomer PDMS (AuNPs–AgNWs/PDMS) as a conductor. The arrayed transistors exhibited reasonably high uniformity in mobility. Logic gates from the integrated transistors in fully rubbery formats were developed. The transistors and logic gates retained their electrical characteristics when stretched by 50%. A fully elastic rubbery tactile sensing skin with a transistor array–based active matrix was further developed so as to illustrate the application of these high-performance rubbery integrated electronics. The electronics and integrated functional devices described here could lead to the development of highly hierarchical and complex rubbery integrated circuits and stretchable integrated functional systems.

<sup>1</sup>Materials Science and Engineering Program, University of Houston, Houston, TX 77204, USA. <sup>2</sup>Department of Mechanical Engineering, University of Houston, Houston, TX 77204, USA. <sup>3</sup>School of Mechanical and Aerospace Engineering, Gyeongsang National University, 501, Jinju-daero, Jinju, Gyeongnam 52828, Korea. <sup>4</sup>Department of Electrical and Computer Engineering, University of Houston, Houston, TX 77204, USA. <sup>5</sup>Department of Biomedical Engineering, University of Houston, Houston, TX 77204, USA.

\*Corresponding author. Email: cy15@uh.edu

## RESULTS

**Rubbery transistor based on a high mobility intrinsically stretchable semiconductor**

Figure 1A shows an optical microscopy image of one rubbery transistor from an array with a AuNPs-AgNWs/PDMS elastomeric conductor as the source and drain electrodes, m-CNT-doped P3HT-NFs/PDMS composite as the semiconducting material, and ion gel as the gate dielectric. We prepared the AuNPs-AgNWs/PDMS elastomeric conductor by embedding AgNWs in PDMS and then by conformally coating the surface with AuNPs through a galvanic replacement process (fig. S1A). The details of the electrode material preparation appear in the Materials and Methods. This surface decoration reduces the energy barrier between the electrodes and the semiconductor and therefore ensures ohmic contact (20). Figure S1B shows the scanning electron microscopy (SEM) images of the AgNWs/PDMS before and after the AuNP coating. An ion gel was used because of its excellent mechanical stretchability, high specific capacitance, low gate voltage, simple processing, and low cost. The details of material preparation are described in Materials

and Methods. A SEM image of such an ion gel is shown in fig. S2 (20, 26). Note that the porous nature of the polymer allows for efficient ion transportation.

The schematic illustration of a fully rubbery transistor in an exploded view and the charge transport path are shown in Fig. 1B. Since the m-CNT has much higher electrical conductivity (27, 28), the charge carrier transportation in the doped semiconductor can be enhanced. The carrier mobility enhancement mechanism is described in detail below. To retain the stretchable semiconductor's semiconducting properties, the conductive pathway of percolated m-CNTs should be avoided, since it can shorten the source and drain of the transistor. Mixing the m-CNT and P3HT in the solution phase does not lead to a high mobility semiconductor because the crystallinity of the P3HT-NFs drops sharply (29–31), in addition to the challenge in dispersing the m-CNT in the solution. A simple dry transfer method (illustrated in Fig. 1C) was therefore developed to accomplish the doping and the device fabrication, which have been verified as feasible and promising. The fabrication process began with spin coating of a well-dispersed

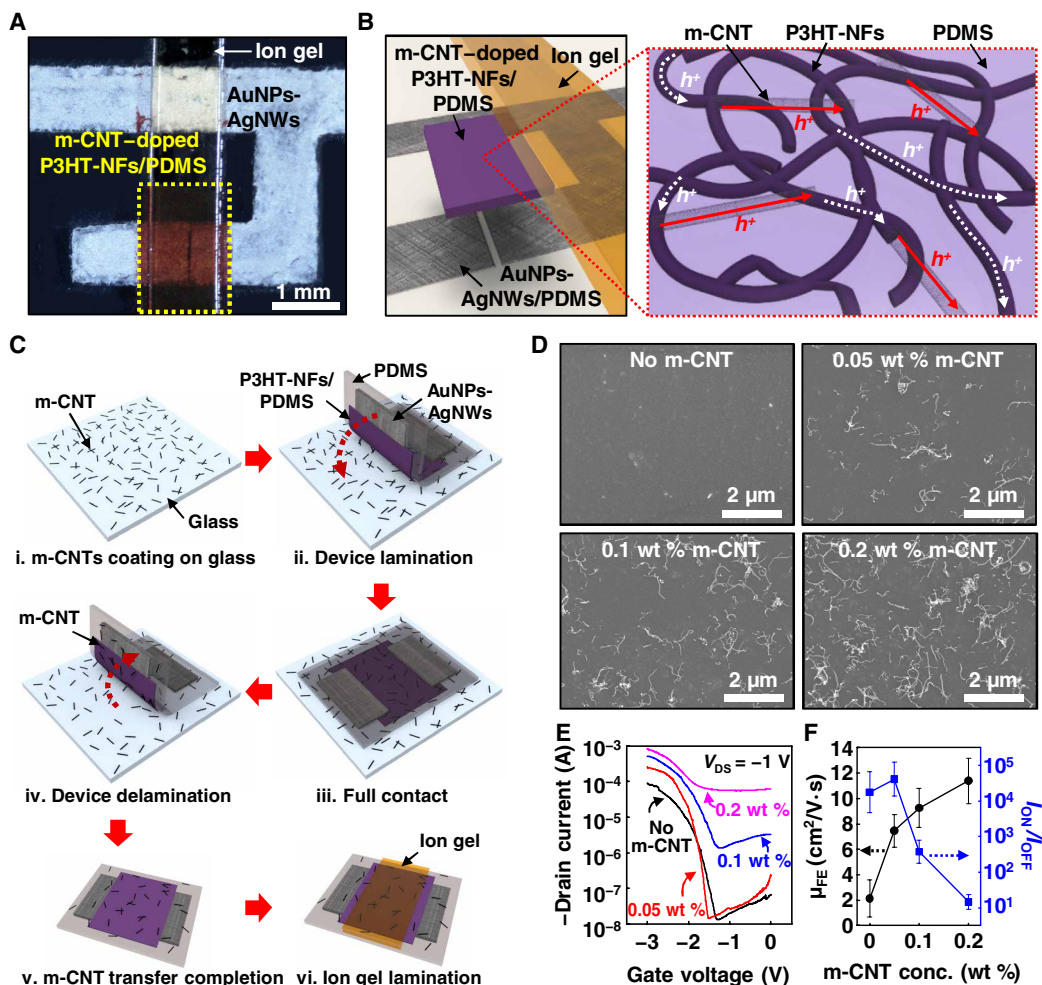


**Fig. 1. High effective mobility intrinsically stretchable semiconductor of m-CNT-doped P3HT-NFs/PDMS-based rubbery transistors.** (A) An optical microscopic image of a rubbery transistor. (B) Schematic exploded view of the rubbery transistor structure and schematic illustration of charge carrier transport routes. (C) Schematic fabrication processes of doping the m-CNT by dry transfer and of constructing the rubbery transistor. (D) SEM images of the m-CNT-doped P3HT-NFs/PDMS semiconducting layer. (E) Transfer characteristics of the devices with different concentrations of the transferred m-CNT. (F)  $\mu_{FE}$  and  $I_{ON}/I_{OFF}$  of the organic transistors with different concentrations of m-CNT.

m-CNT suspension onto a glass slide. Then, a prefabricated transistor with a P3HT-NFs/PDMS-based channel and AuNPs-AgNWs/PDMS-based source and drain electrodes, which we prepared as described in the Materials and Methods (20), was laminated onto the glass slide to form conformal contact. The m-CNTs were transferred onto the surface of the P3HT-NFs/PDMS directly after peeling off the transistor. Last, laminating the free-standing ion gel film completed the device fabrication. Different concentrations of the m-CNT suspension for these high mobility intrinsically stretchable semiconductors were investigated. Figure 1D shows SEM images of the semiconducting layer with the dry-transferred m-CNT with suspension concentrations of 0 (i.e., no m-CNT), 0.05, 0.1, and 0.2 weight % (wt %) that were prepared in 1,2-dichlorobenzene through 1 hour of tip sonication, followed by 5 hours of bath sonication. The area selections with the m-CNTs highlighted in yellow for calculating the areal fraction of m-CNT ( $f_{\text{area,m-CNT}}$ ) are illustrated in fig. S3 (A to C). The linear relationship between the  $f_{\text{area,m-CNT}}$  and the m-CNT concentration of the suspension is shown in fig. S3D. Figure 1E shows the transfer characteristics of the fully rubbery transistors from semiconductors derived with different concentrations of the m-CNTs. The drain current was obtained, while the gate voltage was swept from 0 to  $-3$  V with a constant drain voltage of  $-1$  V. The output characteristics of the devices with different m-CNT concentrations are shown in fig. S4. The m-CNT-doped semiconducting layer showed a significant increase in its  $\mu_{\text{FE}}$  compared with the pristine P3HT-NFs/PDMS composite (0% m-CNT), as illustrated in Fig. 1F. We also experimentally verified that the m-CNT (0.05 wt %) does not form a percolated network. As a further comparison, the nonstretchable semiconductor of the m-CNT-doped P3HT film from spin coating and dry transfer yields an effective  $\mu_{\text{FE}}$  of  $2.55 \text{ cm}^2/\text{V}\cdot\text{s}$ . The transistor transfer characteristics are shown in fig. S5. Figure S6, which shows a detailed comparison of the different semiconductors, suggests that the m-CNT-doped P3HT-NFs/PDMS is the best in terms of high mobility and mechanical stretchability.

The increase in  $\mu_{\text{FE}}$  can be attributed to the fact that m-CNTs provide “fast lanes” for the charge carrier and thus shorten the transport distance in the channel, resulting in higher effective  $\mu_{\text{FE}}$ . In the m-CNT-doped P3HT-NFs/PDMS semiconductor composites, both the m-CNTs and the P3HT-NFs provide paths for the charge carriers to transport between the source and the drain. However, because of the high conductivity of the m-CNTs, the major carrier paths lie in those m-CNTs that bridge the percolated P3HT-NFs. The charge carriers take advantage of the highly conductive pathway in the m-CNT, traveling only a fraction of the distance within the channel and thus leading to reduced channel length and increased effective  $\mu_{\text{FE}}$ . Figure S7A shows the schematic illustration of the charge carrier transport path in the m-CNT-doped P3HT-NFs/PDMS composite. The detailed explanation and analysis of the effective  $\mu_{\text{FE}}$  are presented in the Supplementary Materials. It should be noted that the effective  $\mu_{\text{FE}}$  increase from the m-CNT doping is only feasible if the energy barrier at the junction of the m-CNT and P3HT-NFs is low. A high-energy barrier prevents the charge carriers from transporting effectively. A very low energy barrier of  $\sim 0.1$  eV between the work function of m-CNT (4.8 eV) (32) and the highest occupied molecular orbital energy level of P3HT ( $\sim 4.9$  eV) (33), as schematically shown in fig. S7B, suggests that such a doped semiconductor can yield high effective carrier mobility.

We further experimentally verified the energy barrier between the m-CNT and P3HT-NFs. Since the contact resistance between the semiconductor and the conductor is a direct reflection of the energy barrier (34, 35), we measured the contact resistance of the transistor's electrode and semiconductor. Specifically, we fabricated transistors based on P3HT-NFs/PDMS as the semiconductor and m-CNT as the source and drain electrodes, as shown in fig. S8A. The devices with varied channel lengths from 45 to 370  $\mu\text{m}$  and a fixed channel width of 1000  $\mu\text{m}$  were characterized in the linear regime ( $V_{\text{DS}} \ll V_{\text{GS}} - V_{\text{TH}}$ ) to derive the contact resistance between the m-CNT and the P3HT-NFs through the transfer length method (TLM) (36, 37). The fitting plot of the width ( $W$ ) normalized ON resistance ( $R_{\text{ON}}$ ),  $R_{\text{ON}} \cdot W$ , as a function of the channel length at  $V_{\text{GS}}$  of  $-3$  V and  $V_{\text{DS}}$  of  $-0.2$  V, is shown in fig. S8B. The contact resistance of 270  $\text{ohm}\cdot\text{cm}$  was calculated by extracting the intercept of the TLM plot (36, 37). The details are presented in the Supplementary Materials. In addition, the low-energy barrier between the junction of the m-CNT and the P3HT was also confirmed by the ohmic behaviors in the output characteristics of the transistors with different channel lengths (38, 39), as shown in fig. S8C.

While the intrinsically stretchable semiconductor with more m-CNT dopants has a higher effective  $\mu_{\text{FE}}$ , it should be noted that the off current also increases adversely, which offers a low on/off current ratio (Fig. 1, E and F). On the basis of our experiment, the m-CNT suspension of 0.05 wt % rendered a very high average  $\mu_{\text{FE}}$  ( $7.45 \text{ cm}^2/\text{V}\cdot\text{s}$ ) and an on/off ratio of  $4.11 \times 10^4$  with reasonable reliability, which was therefore chosen for the integrated electronics. It is noted that although this work primarily focuses on P3HT-NFs/PDMS rubbery composite, other semiconductors can possibly exhibit enhanced effective mobility by adding these metallic fast lanes.

### Fully rubbery transistor array

An array (8 by 8) of rubbery transistors fabricated on the basis of the solution process is shown in Fig. 2A. The detailed fabrication process is described in the Materials and Methods and is schematically illustrated in fig. S9. The representative output and transfer curves are exhibited in Fig. 2 (B and C, respectively), showing typical p-channel transistor characteristics. We note that we observed slight hysteresis (fig. S10) by scanning the gate voltage forward and backward. This hysteresis from the ion gel-gated transistor is similar to those reported elsewhere (40, 41), which can be further improved by reducing the thickness of semiconducting layer and scan rate (42). The transistors can be repeatedly fabricated, and the devices in the array operated normally and reliably with a high yield of 100% (Fig. 2D). We calculated the  $\mu_{\text{FE}}$  and  $V_{\text{TH}}$  of the transistors on the basis of the linear regime of these transfer curves (see the Supplementary Materials for details). The highest  $\mu_{\text{FE}}$  in the array is  $9.76 \text{ cm}^2/\text{V}\cdot\text{s}$ , and the average  $\mu_{\text{FE}}$  is  $7.30 \text{ cm}^2/\text{V}\cdot\text{s}$ . Note that we calculated  $\mu_{\text{FE}}$  on the basis of the specific capacitance of the ion gel of  $10.7 \mu\text{F}/\text{cm}^2$  at 1 Hz (43). The average threshold voltage ( $V_{\text{TH}}$ ) and the average on/off current ratio are  $-1.90$  V and  $1.23 \times 10^4$  (fig. S11), respectively. Figure 2E shows various modes of mechanical deformation of the rubbery transistor array, including stretching, poking, and crumpling. Given the rubbery nature of the materials, the transistor array is similar to a piece of rubber and sustains mechanical deformations without any physical damage.

The rubbery transistor's performance under mechanical strain was investigated. We measured its electrical characteristics while applying different levels of mechanical strain both along and perpendicular

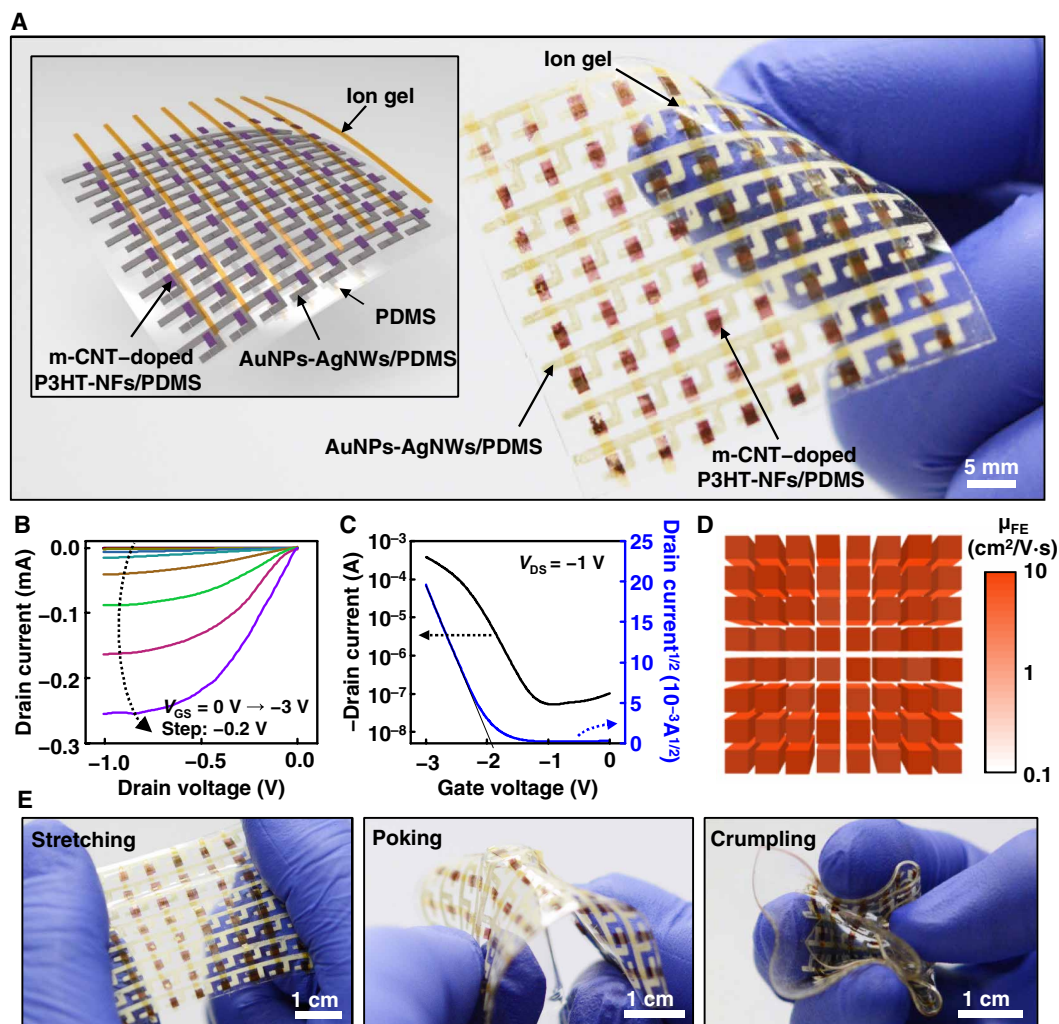


**Fig. 2. Rubbery transistors array.** (A) An optical image of the fabricated high-performance rubbery transistors array. Inset is the exploded schematic view. (B) Representative output characteristics of the m-CNT-doped rubbery transistors. (C) Representative transfer characteristics of the m-CNT-doped rubbery transistors. (D) Calculated  $\mu_{FE}$  map of the 8 by 8 transistor array. (E) Transistor arrays under different mechanical deformation modes.

to the channel length directions. Owing to the rubbery nature of the transistor and associated materials with comparable moduli, we assume the stretching-induced strain to be evenly distributed across the entire device. The optical images of the rubbery transistors under stretching along and perpendicular to the channel length direction are exhibited in Fig. 3 (A and B, respectively). Figure 3 (C and D) shows the transfer curves of the rubbery transistors under 0, 10, 30, 50, and 0% (released) mechanical strains along and perpendicular to the channel length directions, respectively. We calculated and plotted the  $\mu_{FE}$  and  $V_{TH}$  of the rubbery transistor under different levels of mechanical strain in Fig. 3 (E and F, respectively). Note that  $\mu_{FE}$  was calculated on the basis of the deformed channel geometries.

Once the rubbery transistor was stretched by 50% along the channel length direction, a moderate decrease in  $\mu_{FE}$  from  $7.46 \pm 1.37 \text{ cm}^2/\text{V}\cdot\text{s}$  to  $3.57 \pm 1.30 \text{ cm}^2/\text{V}\cdot\text{s}$  and a slight shift in  $V_{TH}$  from  $-2.03 \pm 0.15 \text{ V}$  to  $-1.97 \pm 0.14 \text{ V}$  were obtained. Upon fully releasing the mechanical stretching, both  $\mu_{FE}$  and  $V_{TH}$  recovered to  $5.10 \pm 1.26 \text{ cm}^2/\text{V}\cdot\text{s}$  and  $-1.98 \pm 0.16 \text{ V}$ , respectively (Fig. 3E). Once it was stretched by up to 50% perpendicular to the channel length direction, a relatively larger decrease in  $\mu_{FE}$  from  $7.38 \pm 1.51 \text{ cm}^2/\text{V}\cdot\text{s}$

to  $2.44 \pm 1.19 \text{ cm}^2/\text{V}\cdot\text{s}$  and a slight change in  $V_{TH}$  from  $-1.86 \pm 0.17 \text{ V}$  to  $-1.85 \pm 0.18 \text{ V}$  were observed. Similar to the case of strain along the channel length direction,  $\mu_{FE}$  and  $V_{TH}$  also recovered to  $3.83 \pm 0.72 \text{ cm}^2/\text{V}\cdot\text{s}$  and  $-1.74 \pm 0.15 \text{ V}$ , respectively (Fig. 3F). All these results suggest that high-performance rubbery transistors can maintain normal operation and relatively stable device performances while undergoing a high level of mechanical stretching.

### Rubbery integrated electronics and logic circuits

Logic gates that offer Boolean operations are basic components of integrated electronics and circuits. Integrated electronics in a rubbery format complement conventional rigid electronics technologies and can have many applications that are not easy to achieve with traditional technologies. We developed fully rubbery logic gates, including inverters NAND and NOR, using processes similar to those described above. The rubbery inverter is structured as a zero- $V_{GS}$  load inverter with two p-type stretchable transistors for a unipolar transistor logic gate. Both the driver and load transistors were integrated serially. Figure 4A shows an exploded view of the rubbery inverter. Figure 4B shows an optical image (left) and a circuit diagram

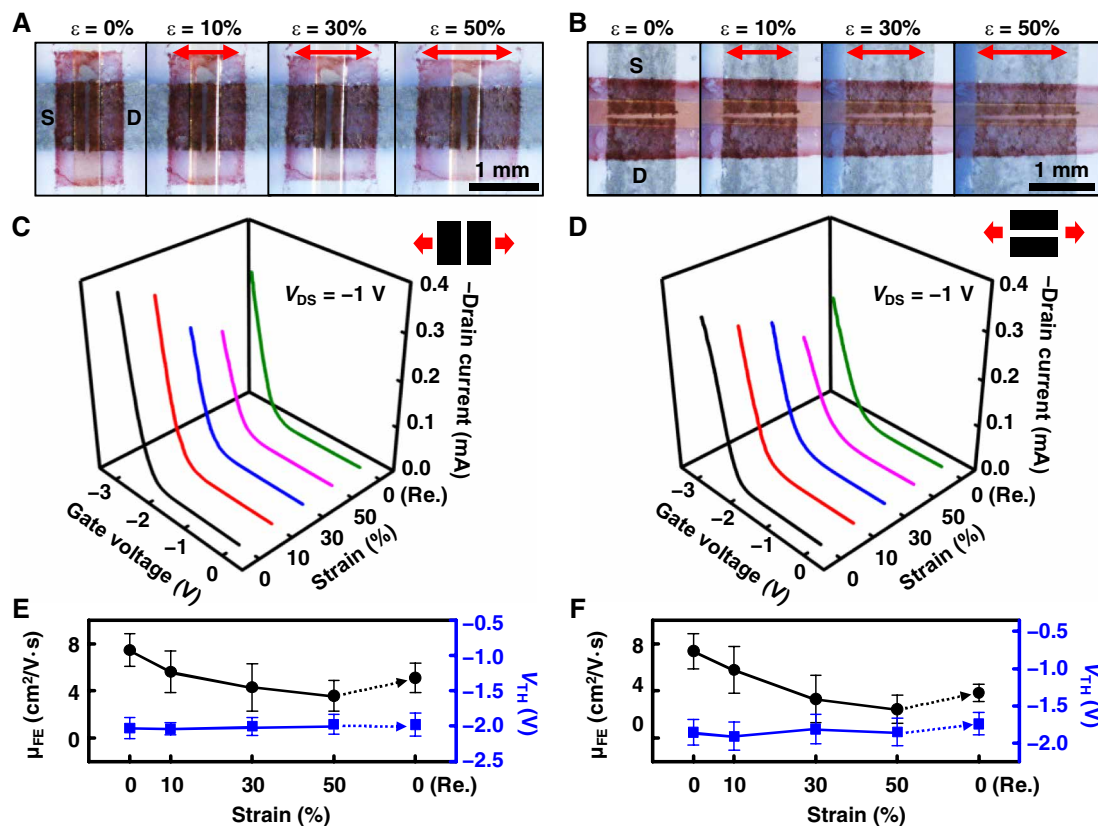


**Fig. 3. Rubbery transistors under mechanical strain.** (A and B) Sequential optical microscopic images of the rubbery transistors under mechanical strains of 0, 10, 30, and 50% along (A) and perpendicular (B) to the channel length direction. (C and D) Transfer characteristics of the rubbery transistors under mechanical strains of 0, 10, 30, 50, and 0% (released) along (C) and perpendicular (D) to the channel length direction. (E and F)  $\mu_{FE}$  and  $V_{TH}$  of the rubbery transistors under mechanical strains of 0, 10, 30, 50, and 0% (released) along (E) and perpendicular (F) to the channel length direction.

(right) of the inverter. Specifically, the two rubbery transistors were designed with a channel width ratio of 1:4 (driver transistor/load transistor) and the same channel length. The voltage transfer curve (VTC) of the inverter was characterized by measuring the output voltage ( $V_{OUT}$ ) under  $V_{DD}$  of 1 V, while the input voltage ( $V_{IN}$ ) was swept from  $-2$  to  $0$  V under mechanical strains of 0, 10, 30, 50, and 0% (released) along and perpendicular to the channel length direction, as shown in Fig. 4 (C and D, respectively). These curves show normal inverter operation with obvious logic output states 1 and 0 under logic input states 0 and 1, respectively. Although the voltage gain and switching threshold voltage ( $V_M$ ) changed slightly under mechanical strain, the values nearly recovered to the initial values (both along and perpendicular to the channel length directional mechanical strain, as shown in Fig. 4E). The hysteresis loop of the inverter is shown in fig. S12, where only slight hysteresis was observed.

We constructed both the rubbery NAND (Fig. 4, F and G) and the NOR (Fig. 4, H and I) gates on the basis of two-driver ( $T_{D,A}$  and  $T_{D,B}$ ) and one-load ( $T_L$ ) rubbery transistors. The two-driver rubbery transistors were connected in parallel for NAND and serially for NOR and then connected serially to the load transistors. The channel lengths of all the driver and load transistors were the same, and the ratios of the channel width of the driver to the load rubbery transistors were 1:4 for the NAND (Fig. 4, F and G) and 1:3 for the NOR gate circuits (Fig. 4, H and I).

The logic function characteristics of the rubbery NAND and NOR logic gates were obtained by measuring  $V_{OUT}$  with a constant

$V_{DD}$  of 1 V under a mechanical strain of 0 and 50% along and perpendicular to the channel length direction. The input voltages ( $V_{IN}$ ) of  $-2$  or  $0$  V for both  $V_{IN,A}$  and  $V_{IN,B}$  represent logic states 0 and 1, respectively. The measured  $V_{OUT}$  of the rubbery NAND gate under no strain is shown in Fig. 4J, which shows logic state 0 only when both inputs are logic state 1. Upon stretching by 50% both along and perpendicular to the channel length direction, the rubbery NAND gate operated normally with no substantial change, as shown in Fig. 4 (K and L). Similar results in Fig. 4 (M to O) show normal operation under no strain and a strain of 50% along both directions for the rubbery NOR gate, which shows logic state 1 only when both inputs are logic state 0. The truth tables for both the rubbery NAND and NOR gates are summarized in fig. S13. Figure S14 shows the static VTC results for both the NAND and NOR logic gates. These results indicate that the fully rubbery logic gates can be stretched without disturbing the Boolean operations.

### Rubbery tactile sensing skin with active matrix electronics

We further demonstrated the use of our high-performance rubbery transistor for a stretchable sensing system to illustrate its further application capabilities. Specifically, a fully rubbery tactile sensing skin with an 8 by 8 active matrix readout was developed. Figure 5A shows the schematic exploded view of the active matrix tactile sensing skin with its key components of rubbery transistors and a pressure-sensitive rubber sheet. The detailed cross-sectional configurations of the rubbery transistor and the pressure-sensitive rubber sheet are schematically

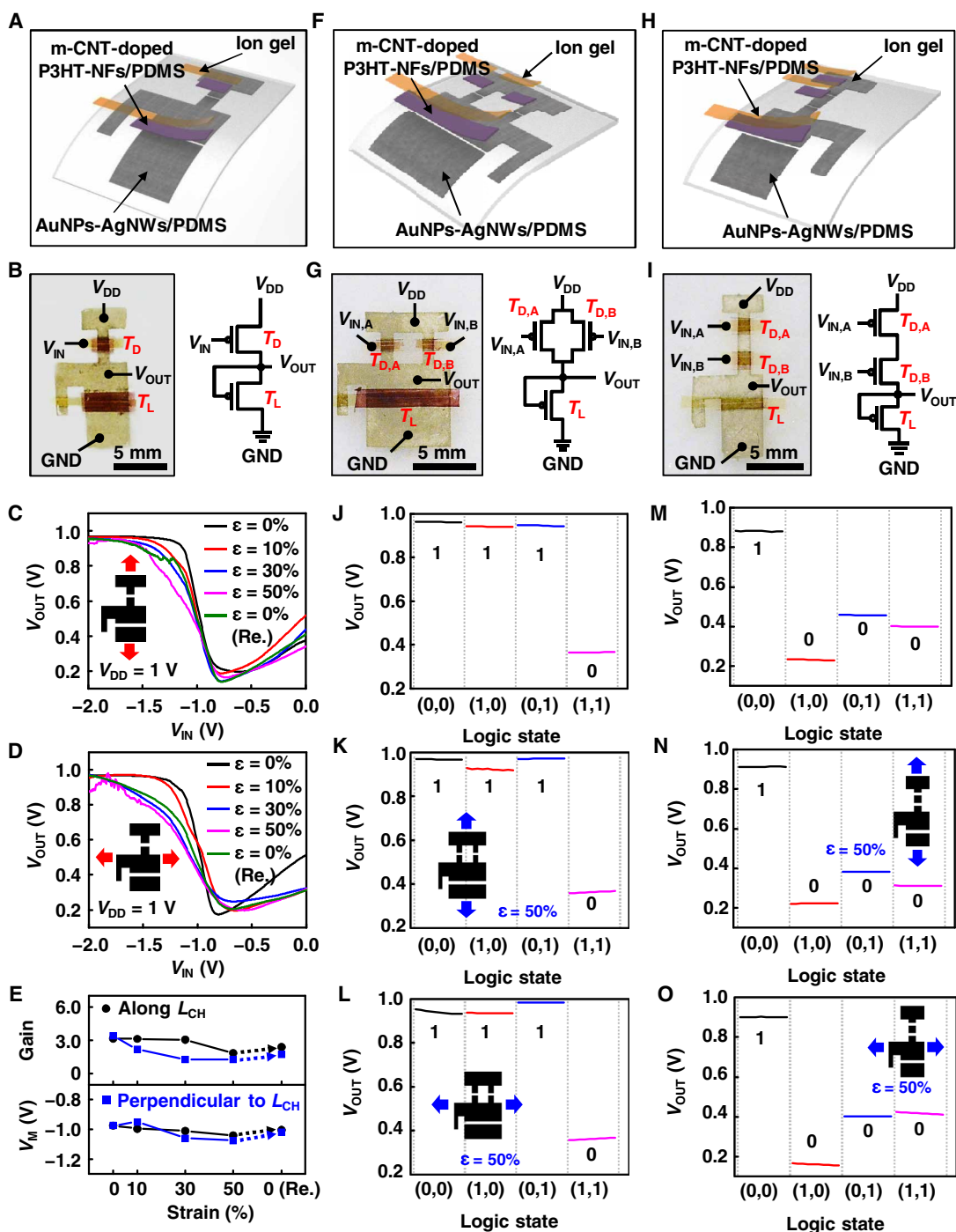


**Fig. 4. Rubbery logic gates.** (A) Exploded schematic illustration of the rubbery inverter. (B) An optical image (left) and a circuit diagram (right) of the rubbery inverter. (C) VTC of the rubbery inverter under mechanical strains of 0, 10, 30, 50, and 0% (released) along the channel length direction. (D) VTC of the rubbery inverter under mechanical strains of 0, 10, 30, 50, and 0% (released) perpendicular to the channel length direction. (E) Voltage gain and  $V_m$  of the rubbery inverter under mechanical strains of 0, 10, 30, 50, and 0% (released) along and perpendicular to the channel length direction. (F) Schematic exploded view of the rubbery NAND gate. (G) An optical image (left) and circuit diagram (right) of the rubbery NAND gate. (H) Schematic exploded view of the rubbery NOR gate. (I) An optical image (left) and circuit diagram (right) of the rubbery NOR gate. (J to L) Output characteristics of the rubbery NAND gate under  $V_{DD}$  of 1 V under mechanical strains of 0% (J) and 50% along (K) and perpendicular (L) to the channel length direction. (M to O) Output characteristics of the rubbery NOR gate under  $V_{DD}$  of 1 V under mechanical strains of 0% (M) and 50% along (N) and perpendicular (O) to the channel length direction.

shown in fig. S15A. The detailed fabrication process is described in the Materials and Methods and is schematically illustrated in fig. S16. Figure S15 (B and C) shows optical images of the interconnected conductive rubber paste and AuNPs-AgNWs/PDMS. Figure 5 (B and C) shows representative mechanical deformation of the active matrix rubbery tactile sensing skin including bending and stretching, respectively. The circuit diagram of an individual tactile sensing pixel is shown in Fig. 5D. The gate electrodes of each column were connected to a word line ( $V_{WL}$ ), and the source electrodes of each row were connected to a bit line ( $V_{BL}$ ). The drain electrodes of each rubbery transistor were supplied with  $V_{DD}$ . The measured drain current ( $I_{DS}$ ) versus the gate voltage ( $V_{GS}$ ) with and without pressing are shown in Fig. 5E.

The resistance of the pressure-sensitive rubber sharply decreased from several hundred megohms to several ohms once the applied pressure exceeded the threshold ( $\sim 100$  kPa; fig. S17), as shown in fig. S18 (A and B). As the skin was pressed, the measured current increased. No cross-talk between the adjacent sensing pixels was observed, where the verification experiment was performed (see the Supplementary Materials for details) and illustrated in fig. S18 (C and D). A quantitative map to exhibit the contact sites was obtained with a data acquisition system (DAQ; National Instruments). The circuit diagram of a fully rubbery tactile sensing skin with an 8 by 8 active matrix is shown in fig. S19. The detailed electrical interfaces with an external DAQ (National Instruments) are described in the

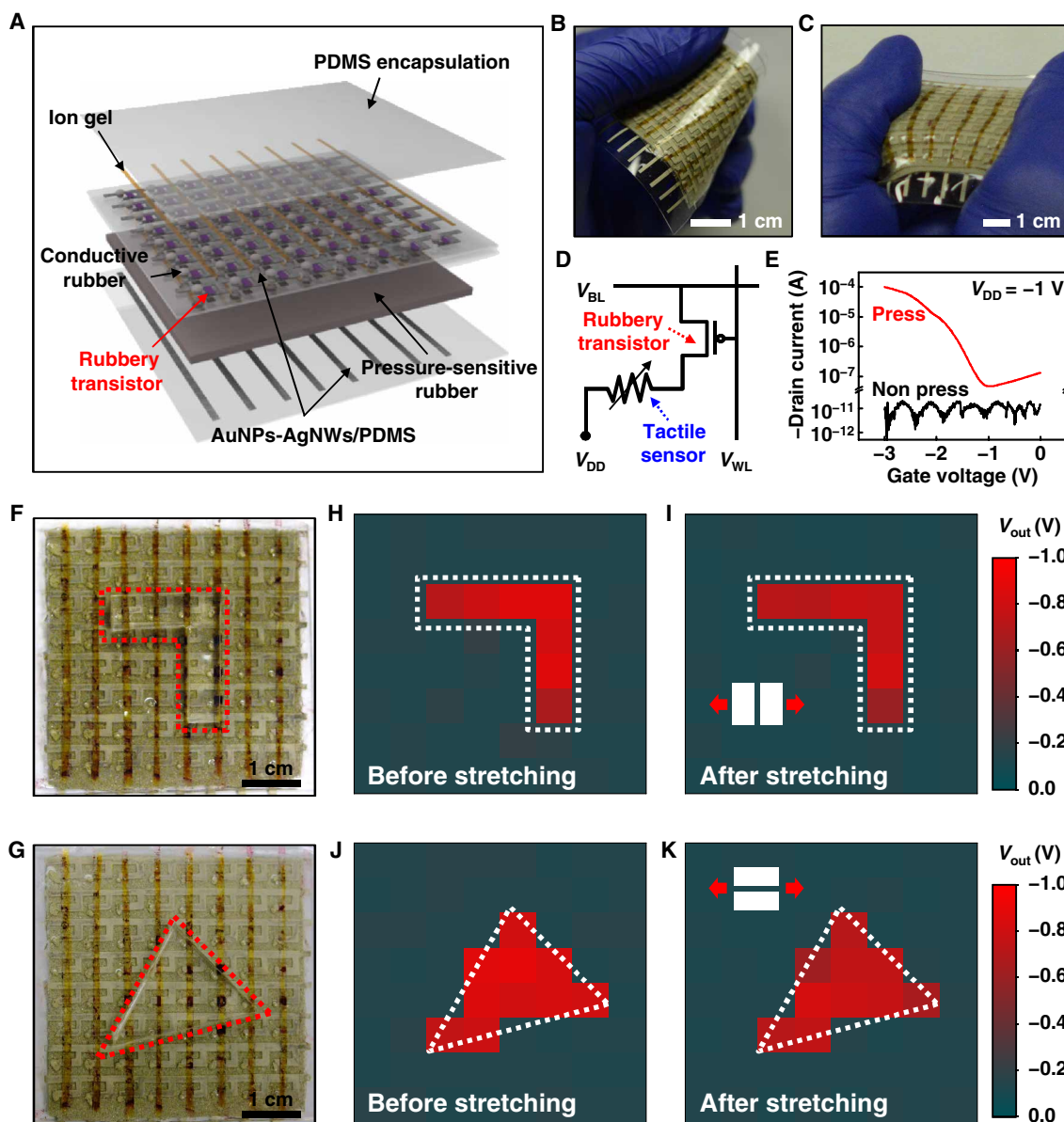


**Fig. 5. Fully rubbery tactile sensing skin with an 8 by 8 active matrix.** (A) Schematic exploded view of the fully rubbery tactile sensing skin. (B and C) The optical images of the deformed fully rubbery tactile sensing skin under bending (B) and stretching (C). (D) The circuit diagram of one tactile sensing pixel. (E) Transfer characteristics of the rubbery transistor in the active matrix with and without applying pressure. (F and G) Optical image of the fully rubbery skin in contact with the custom made rubber block. (H and I) Output voltage mapping result before (H) and after (I) stretching along the channel length direction. (J and K) Output voltage mapping result before (J) and after (K) stretching perpendicular to the channel length direction.

Supplementary Materials. We note that during the readout,  $V_{DD}$  of  $-1$  V and  $V_{GS}$  of  $-3$  V as a word line were supplied. Figure 5 (F and G) shows two examples of touching with pressure applied through objects as indicated in the red dashed areas. The circuit diagram for output voltage measurement and the dynamic output voltage change during cyclic pressing and releasing of a single cell are shown in fig. S20 (A and B, respectively). Figure 5 (H and J) shows the map of the output voltage obtained from each pixel, indicating that the pressed pixels had high voltage. The active matrix was further stretched by 30% and released along and perpendicular to channel length direction. The measured output voltages (Fig. 5, I and K) show no substantial change when the skin is stretched along both directions. The tactile mapping capabilities remained reliable even after more than 100 cycles of stretching and releasing.

## DISCUSSION

Fully rubbery electronics from a high effective mobility intrinsically stretchable semiconductor are realized. The strategy of using m-CNT doping to substantially enhance the effective mobility of the intrinsically stretchable semiconductor proves to be feasible. Our rubbery semiconductor of m-CNT-doped P3HT-NFs/PDMS compared with previously reported intrinsically stretchable polymer semiconductors has clear merits, including much higher  $\mu_{FE}$ , fabrication from commercially available materials, and scalability and repeatability in material and device manufacturing. The demonstrated integrated electronics, logic gates, and sensory skins from these high effective mobility rubbery semiconductors suggest that integrated electronics in a fully rubbery format, in contrast to traditional rigid and brittle counterparts, can be developed. The demonstrated high effective mobility rubbery semiconductors and fully rubbery integrated electronics pave the way toward fully rubbery stretchable functional systems with rubber-like or skin-like mechanical properties in the broad areas of bioelectronics, wearable systems, and large-scale integrated circuits.

## MATERIALS AND METHODS

### Materials

Anhydrous 1,2-dichlorobenzene (>99%), acetone (>99.9%), regio-regular P3HT, multiwalled CNTs (material category, 724769; outer diameter, 6 to 9 nm; length, 5  $\mu$ m; purity, >95%; conducting type, metallic), poly(vinylidene fluoride-co-hexafluoropropylene) (PVDF-HFP; molecular weight,  $\sim$ 400,000), 1-ethyl-3-methylimidazolium bis(trifluoromethylsulfonyl)amide (EMI-TFSA; >98%), gold chloride trihydrate ( $\text{HAuCl}_4 \cdot 3\text{H}_2\text{O}$ ; >99.9%), and anhydrous ammonia ( $\text{NH}_4\text{OH}$ ; 28%) were all from Sigma-Aldrich and used as received. AgNW ( $\sim$ 99.5%) solution (average diameter, 120 nm; length, 20  $\mu$ m) was from ACS Material. Pressure-sensitive rubber sheets (ZL45.1) and conductive rubber pastes (FL45) were from Zoflex. PDMS rubber (Sylgard 184 silicone elastomer kit) was from Dow Corning.

### Preparation of P3HT-NFs/PDMS composite

P3HT was dissolved in the dichloromethane (2 mg/ml) at 60°C and then cooled down to  $-20^\circ\text{C}$  and the solution was kept for 30 min to form P3HT-NFs. The P3HT-NFs solution was blended with a diluted PDMS [10:1 (w/w) prepolymer/curing agent] solution in dichloromethane to obtain the P3HT-NFs/PDMS at the weight ratio of 2:8.

A thin film rubber-like P3HT-NFs/PDMS-percolated nanocomposite semiconductor was accomplished by spin casting and curing at 90°C for 30 min.

### Preparation of stretchable AuNPs-AgNWs/PDMS electrode

To prepare the AuNPs-AgNWs/PDMS composite electrode, the AgNWs were patterned through drop casting the AgNW solution (concentration, 15 mg/ml) onto a clean glass slide with a shadow mask that was manufactured by a programmable cutting machine (Silhouette Cameo) and dried for 10 min at 60°C. Thereafter, the patterned AgNWs on glass were heated at 200°C for 30 min to enhance their electrical conductivity. PDMS solution [10:1 (w/w) prepolymer/curing agent] was then spin-coated onto the patterned AgNWs at 300 rpm for 60 s, followed by a curing process for 4 hours at 60°C for solidification. Relatively high viscosity of the PDMS solution led to only partial permeation through the porous structured AgNWs, resulting in AgNWs partially embedded within the solidified PDMS. The solidified PDMS with AgNWs was then peeled off from the glass slide to achieve stretchable electrodes of AgNWs/PDMS. AuNP coating on the exposed AgNWs involved immersing AgNWs/PDMS composite electrode in 0.5 mM  $\text{HAuCl}_4 \cdot 3\text{H}_2\text{O}$  aqueous solution for 2 min to allow for the Ag-Au galvanic replacement process to take place. The coated electrodes were rinsed with deionized (DI) water and dipped in  $\text{NH}_4\text{OH}$  solution (28%) for 1 min to dissolve the by-products of AgCl layer that were formed on the NWs. The fabrication of the AuNPs-AgNWs/PDMS stretchable electrode was completed by rinsing in DI water, drying with a  $\text{N}_2$  gun, and dehydrating through heating at 90°C for 2 min.

### Preparation of ion gel dielectric

The preparation of the ion gel dielectric began with mixing PVDF-HFP, EMI-TFSA, and acetone in a weight ratio of 1:4:7 at 70°C for 1 hour. The prepared solution was casted on a clean glass substrate and cured in vacuum oven at 70°C for 12 hours to solidify. The solidified ion gel can be easily cut into various shapes and handled. The thickness of the ion gel was approximately 150  $\mu$ m.

### Fabrication of rubbery transistors, transistors array, inverter, NAND, and NOR gates

The fabrication steps of the rubbery transistor involved first creating the AuNPs-AgNWs/PDMS stretchable conductor-based source and drain electrodes, then fabricating the high mobility intrinsically stretchable semiconductor, and lastly laminating the ion gel dielectric. The patterning of the semiconductor was achieved by spin casting through a Kapton film-based shadow mask, followed by annealing for 30 min at 90°C. Specifically, the m-CNT was dispersed in 1,2-dichlorobenzene by ultrasonically the solution for 1 hour with consecutive tip sonication, followed by 5 hours of bath sonication. The m-CNT suspension was spin-coated on a glass slide at 3000 rpm for 60 s and dried at 90°C for 10 min. Thereafter, the P3HT-NFs/PDMS-coated AuNPs-AgNWs/PDMS electrodes were made to laminate and contact with the m-CNT-coated glass, followed by peeling off from the glass to allow for the successful dry transfer of m-CNT onto the semiconductor active layer.

### Fabrication of transistor-based active matrix for sensory skin

The rubbery active matrix transistor fabrication followed the same steps as described above. Via holes were created to allow the



interconnection between the rubbery transistor pixel and the pressure-sensitive rubber sheet placed on the backside of the active matrix. The via holes were filled by conductive rubber paste, which solidified at room temperature for 12 hours. It is noted that the conductive rubber paste and pressure-sensitive rubber strongly adhered to each other, and no delamination was found when they were stretched by 50%. A thin layer of PDMS [10:1 (w/w) prepolymer/curing agent] was spin-coated onto the active matrix as a top encapsulation layer. The rubbery sensory skin was accomplished by laminating a patterned AgNWs/PDMS electrode array to be connected with  $V_{DD}$ .

### Electrical characterization

The surface morphology of the m-CNT-doped P3HT-NFs/PDMS composite, AuNPs-AgNWs/PDMS composite, and ion gel was examined with SEM (XL-30S FEG, Philips). Electrical characterization of the devices was performed with a probe station (H100, Signatone) equipped with a semiconductor characterization system (4200-SCS, Keithley Instruments Inc.). A power supply (GPS-3303, GW Instek) was used to apply external voltage for the inverter, NAND, and NOR characterization. The active matrix tactile sensing skin was characterized via DAQ (NI PXIE-1073 with NI PXIE-6273 and NI PXI-6363; National Instruments). The voltage mapping of touching on the rubbery skin was obtained when applying pressure from a finger onto a piece of a custom-made rubber block.

### SUPPLEMENTARY MATERIALS

Supplementary material for this article is available at <http://advances.sciencemag.org/cgi/content/full/5/2/eaav5749/DC1>

Section S1. Analysis of enhanced effective mobility in m-CNT-doped P3HT-NFs/PDMS  
 Section S2. Contact resistance analysis through the TLM  
 Section S3. Calculation of mobility and threshold voltage  
 Section S4. Circuit architecture designs of the rubbery inverters NAND and NOR  
 Section S5. Cross-talk evaluation of the pressure-sensitive rubber  
 Section S6. Data acquisition of active matrix rubbery tactile sensing skin  
 Fig. S1. Preparation of AgNWs-AuNWs/PDMS through a galvanic replacement process.  
 Fig. S2. SEM image of ion gel.  
 Fig. S3. Areal fraction of m-CNT on the semiconducting layer after dry transfer.  
 Fig. S4. Output characteristics of the devices with different m-CNT concentrations.  
 Fig. S5. Transfer characteristics of the devices with P3HT/m-CNT and P3HT-NFs/PDMS/m-CNT.  
 Fig. S6. Summary list of a few different semiconducting material-based transistors.  
 Fig. S7. Effective  $\mu_{FE}$  enhancement mechanism in m-CNT-doped P3HT-NFs/PDMS.  
 Fig. S8. m-CNT source and drain electrode-based transistor.  
 Fig. S9. Schematic fabrication process of rubbery transistor array.  
 Fig. S10. Hysteresis loop of the transfer curve for the rubbery transistor at a scan rate of 10 mV/s.  
 Fig. S11.  $I_{on}/I_{off}$  map of all 64 rubbery transistors for an 8 by 8 array.  
 Fig. S12. Hysteresis loop of the VTC curve for the rubbery inverter at a scan rate of 10 mV/s.  
 Fig. S13. Truth tables for rubbery NAND and NOR gates.  
 Fig. S14. Static output characteristics of the rubbery NAND and NOR gates.  
 Fig. S15. Physical integration of the fully rubbery tactile sensing skin.  
 Fig. S16. Schematic fabrication processes of the rubbery tactile sensing skin with 8 by 8 transistor array based on an active matrix readout.  
 Fig. S17. Resistance change of the pressure-sensitive rubber sheet depending on applied pressure.  
 Fig. S18. Electrical measurement of the pressure-sensitive rubber sheet.  
 Fig. S19. Circuit diagram of the 8 by 8 active matrix-based rubbery tactile sensing skin.  
 Fig. S20. Output voltage measurement of the rubbery tactile sensing skin.  
 Reference (44)

### REFERENCES AND NOTES

1. T. Sekitani, Y. Noguchi, K. Hata, T. Fukushima, T. Aida, T. Someya, A rubberlike stretchable active matrix using elastic conductors. *Science* **321**, 1468–1472 (2008).
2. N. Liu, A. Chortos, T. Lei, L. Jin, T. R. Kim, W.-G. Bae, C. Zhu, S. Wang, R. Pfattner, X. Chen, R. Sinclair, Z. Bao, Ultratransparent and stretchable graphene electrodes. *Sci. Adv.* **3**, e1700159 (2017).
3. Y. Wang, C. Zhu, R. Pfattner, H. Yan, L. Jin, S. Chen, F. Molina-Lopez, F. Lissel, J. Liu, N. I. Babiah, Z. Chen, J. W. Chung, C. Linder, M. F. Toney, B. Murmann, Z. Bao, A highly stretchable, transparent, and conductive polymer. *Sci. Adv.* **3**, e1602076 (2017).
4. S. Lee, A. Nathan, Subthreshold Schottky-barrier thin-film transistors with ultralow power and high intrinsic gain. *Science* **354**, 302–304 (2016).
5. I. G. Lezama, M. Nakano, N. A. Minder, Z. Chen, F. V. Di Girolamo, A. Facchetti, A. F. Morpurgo, Single-crystal organic charge-transfer interfaces probed using Schottky-gated heterostructures. *Nat. Mater.* **11**, 788–794 (2012).
6. N. Maluf, *An Introduction to Microelectromechanical Systems Engineering* (Artech House Inc., 2002).
7. S. Holliday, R. S. Ashraf, A. Wadsworth, D. Baran, S. A. Yousaf, C. B. Nielsen, C.-H. Tan, S. D. Dimitrov, Z. Shang, N. Gasparini, High-efficiency and air-stable P3HT-based polymer solar cells with a new non-fullerene acceptor. *Nat. Commun.* **7**, 11585 (2016).
8. M. Kaltenbrunner, T. Sekitani, J. Reeder, T. Yokota, K. Kuribara, T. Tokuhara, M. Drack, R. Schwodiauer, I. Graz, S. Bauer-Gogonea, S. Bauer, T. Someya, An ultra-lightweight design for imperceptible plastic electronics. *Nature* **499**, 458–463 (2013).
9. Y. Sun, W. M. Choi, H. Jiang, Y. Y. Huang, J. A. Rogers, Controlled buckling of semiconductor nanoribbons for stretchable electronics. *Nat. Nanotechnol.* **1**, 201–207 (2006).
10. D.-Y. Khang, H. Jiang, Y. Huang, J. A. Rogers, A stretchable form of single-crystal silicon for high-performance electronics on rubber substrates. *Science* **311**, 208–212 (2006).
11. J. Kim, M. Lee, H. J. Shim, R. Ghaffari, H. R. Cho, D. Son, Y. H. Jung, M. Soh, C. Choi, S. Jung, K. Chu, D. Jeon, S.-T. Lee, J. H. Kim, S. H. Choi, T. Hyeon, D.-H. Kim, Stretchable silicon nanoribbon electronics for skin prosthesis. *Nat. Commun.* **5**, 5747 (2014).
12. C. Dagdeviren, Y. Shi, P. Joe, R. Ghaffari, G. Balooch, K. Usgaonkar, O. Gur, P. L. Tran, J. R. Crosby, M. Meyer, Y. Su, R. Chad Webb, A. S. Tedesco, M. J. Slepian, Y. Huang, J. A. Rogers, Conformal piezoelectric systems for clinical and experimental characterization of soft tissue biomechanics. *Nat. Mater.* **14**, 728–736 (2015).
13. S. Xu, Z. Yan, K.-I. Jang, W. Huang, H. Fu, J. Kim, Z. Wei, M. Flavin, J. McCracken, R. Wang, A. Badea, Y. Liu, D. Xiao, G. Zhou, J. Lee, H. U. Chung, H. Cheng, W. Ren, A. Banks, X. Li, U. Paik, R. G. Nuzzo, Y. Huang, Y. Zhang, J. A. Rogers, Assembly of micro/nanomaterials into complex, three-dimensional architectures by compressive buckling. *Science* **347**, 154–159 (2015).
14. S. Xu, Y. Zhang, J. Cho, J. Lee, X. Huang, L. Jia, J. A. Fan, Y. Su, J. Su, H. Zhang, H. Cheng, B. Lu, C. Yu, C. Chuang, T.-i. Kim, T. Song, K. Shigetani, S. Kang, C. Dagdeviren, I. Petrov, P. V. Braun, Y. Huang, U. Paik, J. A. Rogers, Stretchable batteries with self-similar serpentine interconnects and integrated wireless recharging systems. *Nat. Commun.* **4**, 1543 (2013).
15. S.-I. Park, Y. Xiong, R.-H. Kim, P. Elvikis, M. Meitl, D.-H. Kim, J. Wu, J. Yoon, C.-J. Yu, Z. Liu, Y. Huang, K.-c. Hwang, P. Ferreira, X. Li, K. Choquette, J. A. Rogers, Printed assemblies of inorganic light-emitting diodes for deformable and semitransparent displays. *Science* **325**, 977–981 (2009).
16. M. Isobe, K. Okumura, Initial rigid response and softening transition of highly stretchable kirigami sheet materials. *Sci. Rep.* **6**, 24758 (2016).
17. A. Lamoureux, K. Lee, M. Shlian, S. R. Forrest, M. Shtein, Dynamic kirigami structures for integrated solar tracking. *Nat. Commun.* **6**, 8092 (2015).
18. T. C. Shyu, P. F. Damasceno, P. M. Dodd, A. Lamoureux, L. Xu, M. Shlian, M. Shtein, S. C. Glotzer, N. A. Kotov, A kirigami approach to engineering elasticity in nanocomposites through patterned defects. *Nat. Mater.* **14**, 785–789 (2015).
19. J. Xu, S. Wang, G.-J. N. Wang, C. Zhu, S. Luo, L. Jin, X. Gu, S. Chen, V. R. Feig, J. W. F. To, S. Rondeau-Gagné, J. Park, B. C. Schroeder, C. Lu, J. Y. Oh, Y. Wang, Y.-H. Kim, H. Yan, R. Sinclair, D. Zhou, G. Xue, B. Murmann, C. Linder, W. Cai, J. B.-H. Tok, J. W. Chung, Z. Bao, Highly stretchable polymer semiconductor films through the nanoconfinement effect. *Science* **355**, 59–64 (2017).
20. H.-J. Kim, K. Sim, A. Thukral, C. Yu, Rubbery electronics and sensors from intrinsically stretchable elastomeric composites of semiconductors and conductors. *Sci. Adv.* **3**, e1701114 (2017).
21. S. Wang, J. Xu, W. Wang, G.-J. N. Wang, R. Rastak, F. Molina-Lopez, J. W. Chung, S. Niu, V. R. Feig, J. Lopez, T. Lei, S.-K. Kwon, Y. Kim, A. M. Foudeh, A. Ehrlich, A. Gasparini, Y. Yun, B. Murmann, J. B.-H. Tok, Z. Bao, Skin electronics from scalable fabrication of an intrinsically stretchable transistor array. *Nature* **555**, 83–88 (2018).
22. D. Choi, H. Kim, N. Persson, P.-H. Chu, M. Chang, J.-H. Kang, S. Graham, E. Reichmanis, Elastomer-polymer semiconductor blends for high-performance stretchable charge transport networks. *Chem. Mater.* **28**, 1196–1204 (2016).
23. G. Zhang, M. McBride, N. Persson, S. Lee, T. J. Dunn, M. F. Toney, Z. Yuan, Y.-H. Kwon, P.-H. Chu, B. Risteen, Versatile interpenetrating polymer network approach to robust stretchable electronic devices. *Chem. Mater.* **29**, 7645–7652 (2017).
24. X. Liu, C. Wang, B. Cai, X. Xiao, S. Guo, Z. Fan, J. Li, X. Duan, L. Liao, Rational design of amorphous indium zinc oxide/carbon nanotube hybrid film for unique performance transistors. *Nano Lett.* **12**, 3596–3601 (2012).
25. H.-C. Liu, Y.-C. Lai, C.-C. Lai, B.-S. Wu, H.-W. Zan, P. Yu, Y.-L. Chueh, C.-C. Tsai, Highly effective field-effect mobility amorphous InGaZnO TFT mediated by directional silver nanowire arrays. *ACS Appl. Mater. Interfaces* **7**, 232–204 (2014).
26. J. Lee, M. J. Panzer, Y. He, T. P. Lodge, C. D. Frisbie, Ion gel gated polymer thin-film transistors. *J. Am. Chem. Soc.* **129**, 4532–4533 (2007).

27. I. D. Rosca, S. V. Hoa, Highly conductive multiwall carbon nanotube and epoxy composites produced by three-roll milling. *Carbon* **47**, 1958–1968 (2009).
28. M. Wang, K. Zhang, X.-X. Dai, Y. Li, J. Guo, H. Liu, G.-H. Li, Y.-J. Tan, J.-B. Zeng, Z. Guo, Enhanced electrical conductivity and piezoresistive sensing in multi-wall carbon nanotubes/polydimethylsiloxane nanocomposites via the construction of a self-segregated structure. *Nanoscale* **9**, 11017–11026 (2017).
29. G.-W. Hsieh, F. M. Li, P. Beecher, A. Nathan, Y. Wu, B. S. Ong, W. I. Milne, High performance nanocomposite thin film transistors with bilayer carbon nanotube-polythiophene active channel by ink-jet printing. *J. Appl. Phys.* **106**, 123706 (2009).
30. C. Derry, Y. Wu, S. Zhu, J. Deen, Composite semiconductor material of carbon nanotubes and poly [5, 5'-bis (3-dodecyl-2-thienyl)-2, 2'-bithiophene] for high-performance organic thin-film transistors. *J. Electron. Mater.* **42**, 3481–3488 (2013).
31. Y. D. Park, J. A. Lim, Y. Jang, M. Hwang, H. S. Lee, D. H. Lee, H.-J. Lee, J.-B. Baek, K. Cho, Enhancement of the field-effect mobility of poly (3-hexylthiophene)/functionalized carbon nanotube hybrid transistors. *Org. Electron.* **9**, 317–322 (2008).
32. M. Shiraishi, M. Ata, Work function of carbon nanotubes. *Carbon* **39**, 1913–1917 (2001).
33. L. Janasz, A. Luczak, T. Marszalek, B. G. R. Dupont, J. Jung, J. Ulanski, W. Pisula, Balanced ambipolar organic field-effect transistors by polymer preaggregation. *ACS Appl. Mater. Interfaces* **9**, 20696–20703 (2017).
34. K. Shibata, K. Ishikawa, H. Takezoe, H. Wada, T. Mori, Contact resistance of dibenzotetrathiafulvalene-based organic transistors with metal and organic electrodes. *Appl. Phys. Lett.* **92**, 023305 (2008).
35. S.-W. Rhee, D.-J. Yun, Metal-semiconductor contact in organic thin film transistors. *J. Mater. Chem.* **18**, 5437–5444 (2008).
36. C. Liu, Y. Xu, Y. Li, W. Scheideler, T. Minari, Critical impact of gate dielectric interfaces on the contact resistance of high-performance organic field-effect transistors. *J. Phys. Chem. C* **117**, 12337–12345 (2013).
37. C. Liu, Y. Xu, Y.-Y. Noh, Contact engineering in organic field-effect transistors. *Mater. Today* **18**, 79–96 (2015).
38. S. J. Kang, G.-H. Lee, Y.-J. Yu, Y. Zhao, B. Kim, K. Watanabe, T. Taniguchi, J. Hone, P. Kim, C. Nuckolls, Organic field effect transistors based on graphene and hexagonal boron nitride heterostructures. *Adv. Funct. Mater.* **24**, 5157–5163 (2014).
39. J.-P. Hong, A.-Y. Park, S. Lee, J. Kang, N. Shin, D. Y. Yoon, Tuning of Ag work functions by self-assembled monolayers of aromatic thiols for an efficient hole injection for solution processed triisopropylsilyl ethynyl pentacene organic thin film transistors. *Appl. Phys. Lett.* **92**, 143311 (2008).
40. B. C. Popere, G. E. Sanoja, E. M. Thomas, N. S. Schausser, S. D. Jones, J. M. Bartels, M. E. Helgeson, M. L. Chabiny, R. A. Segalman, Photocrosslinking polymeric ionic liquids via anthracene cycloaddition for organic electronics. *J. Mater. Chem. C* **6**, 8762–8769 (2018).
41. A. G. Kelly, T. Hallam, C. Backes, A. Harvey, A. S. Esmaeili, I. Godwin, J. Coelho, V. Nicolosi, J. Lauth, A. Kulkarni, S. Kinge, L. D. A. Siebbeles, G. S. Duesberg, J. N. Coleman, All-printed thin-film transistors from networks of liquid-exfoliated nanosheets. *Science* **356**, 69–73 (2017).
42. S. H. Kim, K. Hong, K. H. Lee, C. D. Frisbie, Performance and stability of aerosol-jet-printed electrolyte-gated transistors based on poly (3-hexylthiophene). *ACS Appl. Mater. Interfaces* **5**, 6580–6585 (2013).
43. K. H. Lee, M. S. Kang, S. Zhang, Y. Gu, T. P. Lodge, C. D. Frisbie, “Cut and stick” rubbery ion gels as high capacitance gate dielectrics. *Adv. Mater.* **24**, 4457–4462 (2012).
44. T. Minari, P. Darmawan, C. Liu, Y. Li, Y. Xu, K. Tsukagoshi, Highly enhanced charge injection in thienoacene-based organic field-effect transistors with chemically doped contact. *Appl. Phys. Lett.* **100**, 093303 (2012).

#### Acknowledgments

**Funding:** C.Y. thanks the NSF (ECCS-1509763 and CMMI-1554499), the Doctoral New Investigator grant from American Chemical Society Petroleum Research Fund (56840-DNI7), and the Bill D. Cook Faculty Scholarship from the Department of Mechanical Engineering at University of Houston. The NSF-funded IUCRC BRAIN Center at the University of Houston is also acknowledged for the partial support of this work. **Author contributions:** K.S. and C.Y. conceived and designed the experiment. K.S., Z.R., H.-J.K., A.T., and H.S. performed the experiments. K.S., Z.R., H.-J.K., and C.Y. analyzed the data. K.S. and C.Y. wrote the paper. **Competing interests:** The authors declare that they have no competing interests. **Data and materials availability:** All data needed to evaluate the conclusions in the paper are present in the paper and/or the Supplementary Materials. Additional data related to this paper may be requested from the authors.

Submitted 29 September 2018

Accepted 13 December 2018

Published 1 February 2019

10.1126/sciadv.aav5749

**Citation:** K. Sim, Z. Rao, H.-J. Kim, A. Thukral, H. Shim, C. Yu, Fully rubbery integrated electronics from high effective mobility intrinsically stretchable semiconductors. *Sci. Adv.* **5**, eaav5749 (2019).